minerals

MDPI

Article

Molecular Dynamics Simulation of Methane Adsorption and Diffusion: A Case Study of Low-Rank Coal in Fukang Area, Southern Junggar Basin

Jie Xiang [1,2], Xianqing Li [1,2,*], Weiyu Gao [3], Yu Liu [1,2], Jiandong Li [1,2], Jingwei Yang [1,2] and Yixiao Gong [1,2]

[1] State Key Laboratory of Coal Resources and Safe Mining, China University of Mining and Technology (Beijing), Beijing 100083, China
[2] College of Geoscience and Surveying Engineering, China University of Mining and Technology (Beijing), Beijing 100083, China
[3] Inner Mongolia Geology and Minerals Co., Hohhot 010020, China
* Correspondence: lixq@cumtb.edu.cn; Tel.: +86-10-62331854

Abstract: Adsorption and diffusion are the key factors affecting coalbed methane (CBM) accumulation, resource assessment and production prediction. To study the adsorption and diffusion mechanism of Fukang low-rank coal at the microscopic level, samples of Fukang low-rank coal were collected, and the elemental composition, carbon type distribution and functional group type of the Fukang low-rank coal structure were determined by elemental analysis (Ea), Fourier-transform interferometric radiometer (FTIR), X-ray photoelectron spectroscopy (XPS) and ^{13}C nuclear magnetic resonance (^{13}C NMR) experiments to construct a 2D molecular structure of the coal and a 3D macromolecular structure model. The adsorption and diffusion characteristics of methane were researched by giant regular Monte Carlo (GCMC) and molecular dynamics (MD) simulation methods. The results showed that the excess adsorption amount of methane increased and then decreased with the increase in pressure. The diffusion of methane showed two stages with increasing pressure: a sharp decrease in the diffusion coefficient from 0.5 to 5.0 MPa and a slow decrease in the diffusion coefficient from 5.0 to 15.0 MPa. The lower the pressure, the larger the effective radius of the CH_4 and C atoms, and the higher the temperature, the more pronounced the diffusion and the larger the effective radius.

Keywords: low-rank coal; molecular structure; adsorption; diffusion; molecular dynamics

check for updates

Citation: Xiang, J.; Li, X.; Gao, W.; Liu, Y.; Li, J.; Yang, J.; Gong, Y. Molecular Dynamics Simulation of Methane Adsorption and Diffusion: A Case Study of Low-Rank Coal in Fukang Area, Southern Junggar Basin. *Minerals* **2023**, *13*, 229. https://doi.org/10.3390/min13020229

Academic Editor: Pieter Bertier

Received: 3 January 2023
Revised: 2 February 2023
Accepted: 2 February 2023
Published: 4 February 2023

1. Introduction

The coalbed methane (CBM) resources in China are mainly concentrated in the Qinshui Basin, Ordos Basin and Junggar Basin. The Junggar Basin is one of the most typical coal-bearing basins in China and is rich in low-rank coal and CBM resources, making it a potential alternative area for CBM development. [1–4]. The coal seams in this area are suitably buried, have ultrahigh thickness (>15m) with large dips (>50°) and Ro values of 0.50–0.88% (average 0.65%), and their pore types are mainly microporous and macroporous [5–7]. The structure of coal is an essential parameter affecting CBM production and reservoir augmentation [8]. The desorption isotherm is mainly type B, caused mainly by ink bottles and slit pores, indicating that the area is favorable for CBM enrichment and unfavorable for diffusive seepage [9,10]. The formation of organic matter in coal of different pore sizes generally occurs during the coalification process, which has a direct impact on the extraction of CBM [11], and as the Ro value increases, there is a tendency for the influential water content and volatile content to decrease, the fixed carbon content to increase, the percolation pores to gradually change to adsorption pores, the main pore type to change from mesoporous to micropore and the pore distribution curve to change from bimodal to single peak [12]. The variation in permeability determines to some extent the distribution of gas content, particularly in deep coal reservoirs [6]. Pore pressure and in situ stress are the key factors affecting CBM exploration and development [13]. The methane content of shallower buried coal seams is mainly controlled by formation pressure, while the content of deeper coal seams is mainly controlled by the negative impact of reservoir temperature [14]. The methane content of the coal seam is also influenced by tectonic movement, with complex tectonic zones being low and simple tectonic zones being high, and the greater the dip of the coal seam, the lower the gas content. [15,16]. At present, hydraulic fracturing and liquid nitrogen fracturing are mainly used to exploit coalbed methane, and carbon dioxide, nitrogen or water vapor is injected into the coal seam to replace methane so as to achieve the purpose of increasing coalbed methane production. Although a great deal of previous research has been carried out on the low production of CBM in the southern margin of the Junggar Basin, no one has carried out molecular-scale studies of adsorption–diffusion of CBM for this region, which is considered to be crucial.

Molecular simulation is widely used to construct the molecular structure of coal and study the mechanism of coal and methane interaction at the microscopic level [17–35]. To optimize gas production from coal reservoir rocks, an understanding of diffusion kinetics is a prerequisite [26]. The gas diffusion in the coal matrix is a vital process for mass migration from the pores to the cleats [36,37]. Molecular dynamics simulation is one of the most effective methods to study the microscopic mechanism of adsorbent diffusion [17,25,37–40].

The methane in the coal reservoir is mainly in the adsorbed state and the free state, which can be transformed into each other. As the pore pressure decreases, the methane adsorbed on the coal surface is desorbed, the adsorbed gas is converted into free gas and the gas diffuses from the coal matrix into the cleat system, from where it infiltrates the production well. Previous studies have concluded that coal particles, pores, temperature, pressure and water are the main factors affecting the adsorption and diffusion of methane in coal [21,35,38,39,41–47]. By comparing the adsorption and diffusion of methane, N_2 and CO_2, the loading amounts in pore models increased with increasing pore size, and the larger pores were more conducive to gas diffusion [38]. As the pore size decreases, the self-diffusion coefficient also decreases, and in smaller pores, the molecular motion is weakened overall [48]. In different pores, the magnitude of the transport diffusion coefficient at low pressure is opposite to that at high pressure [48]. Gases have three diffusion coefficients: the self-diffusion coefficient, modified diffusion coefficient and migrating diffusion coefficient. All three different diffusion coefficients increased with increasing temperature, and the transport diffusion coefficient increased and then decreased with increasing pressure, reaching a peak [49]. Temperature and pressure significantly affect the diffusion of gases, where the increase in temperature is beneficial to the diffusion of gas, and the rise in pressure makes the diffusion coefficient increase first and then decrease, reaching the peak value (3.0 MPa) [37]. The increase in moisture within the pore space reduces the sorption properties, and internal moisture is negatively correlated with the self-diffusion and transport diffusion coefficients [41]. Water molecules interfere with the sorption and diffusion of CO_2 and CH_4 [39]. The diffusion coefficient decreases with increasing particle size and increases with increasing pressure and temperature [50]. The diffusion of CH_4 in shales is related to the sorbent's concentration, and the effective diffusion coefficient increases with increasing pressure and decreases with increasing temperature [51]. The diffusion coefficient in hard coals decreases with increasing grain size, while in brittle coals, the diffusion coefficient varies randomly within a small range of values with increasing grain size [52]. The larger the particle size, the slower the initial gas diffusion rate and the longer the time required to reach the desorption equilibrium. The higher the adsorption pressure, the greater the initial gas diffusion rate and the greater the accumulation of diffused gas [43]. Although a large number of previous studies on CH_4 diffusion in coal have been carried out at the molecular level, no one has yet used SWNTs to model the adsorption and diffusion of CH_4 by drilling cylindrical pores of different pore sizes in a macromolecular model of coal.

In summary, in this study, macromolecules of Fukang low-rank coal were obtained by elemental analysis, ^{13}CNMR, FTIR and XPS. The quantitative study of the adsorption and diffusion mechanisms is based on the giant canonical Monte Carlo (GCMC) and molecular dynamics (MD) methods. The objectives of this work are (i) to improve the existing understanding of the diffusion process of CH_4 in coal and (ii) to investigate the relationship between the diffusion kinetics of coal and temperature, pressure and pore size. This relationship can be demonstrated in terms of mean square displacement, diffusion coefficient and atomic radial distribution function (RDF) to show the diffusion characteristics of methane in coal. This study may provide a reliable theoretical basis and foundation for E-CBM to achieve efficient CBM development.

2. Materials and Methods

2.1. Molecular Structure Construction

2.1.1. Sample Collection and Preparation

The experimental coal samples were taken from the intact sidewalls of the key exploration wells FSG-1, FSG-2, FSG-3 and FSG-4 in Fukang mining area in the southern margin of the Junggar Basin and were Jurassic Badaowan Formation coal with a sampling depth of 865–985m (Figure 1). Coal core sampling complied with the national standard GB/T 482–2008. The samples were first cracked, ground into tiny particles using agate mortar, sieved to 100–200 mesh size, dried at 105 °C for 24 h using a blower and then loaded into plastic bags. Then, the coal samples were subjected to element analysis, FTIR spectroscopy, XPS experiment and ^{13}C NMR measurement.

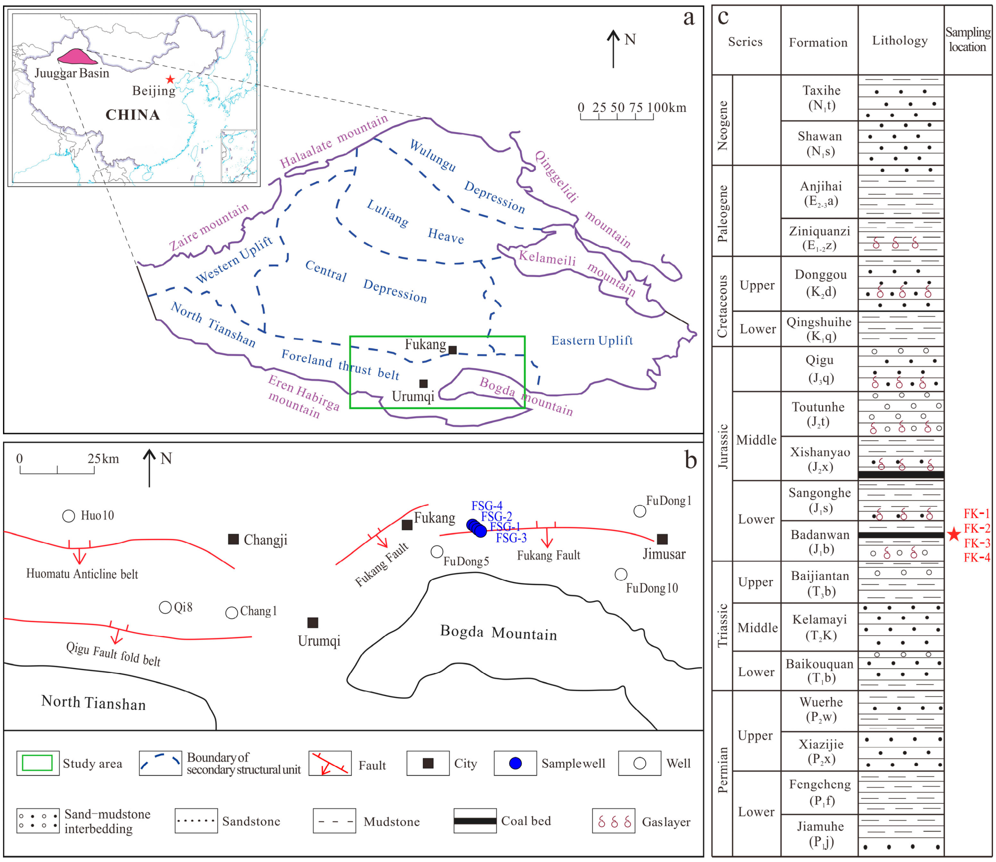

Figure 1. Geographic location, Sampling locations and lithological column: (**a**) location of the Junggar Basin, (**b**) location of the study area, and (**c**) the lithological column.

2.1.2. Proximate Analysis and Ultimate Analysis

We tested the samples for organic elements using Elementar vario el III (Vario EL III, Elementar, Hanau, Germany), and the test mode was CHNS mode/O mode. The total sulfur content of the coal samples was determined according to the national standard "Determination of total sulfur in Coal" (GB/T 214-2007); the carbon, hydrogen and nitrogen content of the coal samples were determined according to the national standard "Determination of Carbon and Hydrogen in Coal" (GB/T 476-2008) and "Determination of Nitrogen in Coal" (GB/T 19227-2008). The moisture, ash and volatile contents of the coal samples were determined according to the national standard "Proximate Analysis of Coal" (GB/T 212-2008).

2.1.3. FTIR Spectroscopy

Spectral analysis can be used to determine the presence of compounds or functional groups in the sample. The absorption peaks of the infrared spectrum of coal can be divided into four types: (1) the absorption peaks of coal at 700~900 cm^{-1} are an aromatic structure; (2) the absorption peaks of coal at 1000~1800 cm^{-1} are an oxygen-containing functional group; (3) the range from 2800 to 3000 cm^{-1} is the stretching vibration absorption band of aliphatic hydrocarbon CH_x; and (4) the hydroxyl group has an absorption peak between 3000 and 3600 cm^{-1} [53].

The Fourier-transform interferometric radiometer (FTIR) test was carried out on a Thermo Scientific Nicolet iS10 (FTIR, Thermo Fisher Scientific, Waltham, USA) with a potassium bromide press. The test procedure was to take $1-2$ mg of a powder sample and 200 mg of pure KBr, grind it evenly, put it in a mold, press it into a transparent slice on a hydraulic press, put the sample into an infrared spectrometer and test it in the wave number range 4000~400 cm^{-1}, scan number 32, resolution 4 cm^{-1}.

2.1.4. XPS Experiment

XPS is an experimental tool for quantifying information about the different chemical functional groups in the structure of coal and is often used to characterize the chemical structure of organic matter [18,54–56]. The instrument used for the X-ray photoelectron spectroscopy (XPS) experiments was Thermo Scientific K-Alpha (XPS, Thermo Fisher Scientific, Waltham, MA, USA). The excitation source was Al Kα rays (6 eV), the bunch spot was 400 µm, the analysis chamber vacuum was ~3×10^{-7} mba, the full spectrum scan used a pass energy of 150 eV and a step size of 1 eV and binding energy correction used surface contamination C 1s (284.8 eV) as a standard.

2.1.5. ^{13}C NMR Measurement

^{13}C NMR has been shown to verify the chemical shifts of functional groups in the structure of coal, with different functional groups having different chemical shifts [57,58]. The solid-state dipolar decoupling magic angle spinning (DD/MAS) ^{13}C nuclear magnetic resonance (^{13}C NMR) measurement was performed using the JNM-ECZ600R spectrometer manufactured by JEOL Company (Shoshima City, Tokyo, Japan). The tube diameter is 3.2 mm and has a frequency of 150 MHz; the mas frequency is 12 KHz, the relaxation delay is 5 s, the scans are 700 and seven hundred scans over a total experimental time of one hour were used.

2.1.6. Fukang Coal Molecular Structure Construction

Construction of the chemical structure of Fukang coal has been based mainly on experimental results from ^{13}C NMR and XPS measurements. FTIR spectroscopy has also been used to verify certain chemical functional groups such as –C=O, –OH, $-CH_2$ and $-CH_3$ [18,54,59]. XPS analysis data allow estimation of the relative content of individual atoms in a molecule and determination of the relative content of different groups of heteroatoms. ^{13}C NMR spectroscopy allowed the relative content of aliphatic and aromatic carbons to be estimated [18]. These clusters were stitched together to create the initial primary coal macromolecules, and the ^{13}C NMR of the created 2D coal macromolecules was calculated using ACD/C-NMR prediction software (version 10.04). gNMR software (version 5.0.6.0) was then used to compare the calculated NMR spectra with the experimental NMR spectra. The coal macromolecules were continually adjusted until the NMR data of the final macromolecular structure were in general agreement with the experimental NMR data. This method has been widely used to construct coal and cuticle macromolecules and is correct and demonstrated to be reliable [18,19,52]. Then, the 2D chemical structure model was imported into Materials Studio software, and the energy optimization, geometric optimization and annealing dynamics simulation were carried out in the Forcite module to build the 3D model of Fukang coal. In the amorphous cell module, multiple 3D coal molecules were loaded into a crystal cell with periodic boundary, and energy optimization, geometric optimization and annealing dynamics simulation were carried out again to establish the 3D macromolecular structure of Fukang coal.

2.2. Adsorption Simulation Method

Coal is a nonhomogeneous porous media material with complex chemical and physical properties [38]. According to the classification of coal pore size by the International Union of Pure and Applied Chemistry (IUPAC), less than 2 nm is considered microporous and 2–50 nm is mesoporous, while 50–100 nm is considered macroporous. Micropores and mesoporous pores in coal are the main adsorption sites for methane. In this paper, we used the 3D macromolecular structure as a basis, a 1 nm blank slit layer was constructed and the adsorption behavior of methane was studied using the large canonical ensemble Monte Carlo (GCMC) simulation method using the adsorption module in Materials Studio software (version 19.1.0.2353) [46,60].

The saturation adsorption of methane is performed in the sorption module in Material Studio. The task is fix pressure, the method is Metropolis, the quality is acceptable, the equilibration steps are 100,000, the production steps are 1,000,000, the forcefield is COMPASS, the charges are forcefield assigned and the electrostatic is Ewald. The diffusion of methane is executed in the Forcite module of Material Studio, where the task is dynamics, the quality is fine, the time step is 1.0 fs, the total simulation time is 500 ps and the number of steps is 500,000. The frame output is every 5000 steps, and the NVT system and the NVE system were successively used in the optimization process. The calculation was carried out using analysis of the Forcite module after optimization. The mean square displacement curves for different systems can be obtained.

Fugacity is the pressure of an ideal gas with the same chemical potential under the same conditions. In this study, we used REFPROP software (REFPROP is a fluid thermodynamics and transport properties database from the National Institute of Standards and Technology. Its full name is Reference Fluid Thermo-dynamic and Transport Properties Database) to calculate the fugacity coefficient of methane at different temperatures and pressures. Then, we calculated the fugacity values by Equation (1).

$$f_i = \varphi_i \cdot P_i \tag{1}$$

where f_i is fugacity, MPa; φ_i is the fugacity coefficient; and P_i is pressure, MPa.

The methane adsorption simulated by Materials Studio software is the absolute adsorption amount, while the adsorption capacity obtained in the experiment is the excess adsorption amount. In the simulation, He atom with poor adsorption capacity was used as the probe to calculate the self-use space volume. REFPROP software is also used to calculate the methane density under different temperatures and pressures. The excess adsorption amount can be obtained by Equation (2).

$$N_{ex} = N_{ad} - \rho_g \cdot V_P \tag{2}$$

where N_{ex} is the excess adsorption amount, mmol/g; N_{ad} is the absolute adsorption amount, mmol/g; ρ_g is the methane density at a certain temperature and pressure, g/cm^3; and V_P is the pore volume, cm^3.

2.3. Molecular Dynamics Simulation

Supercell extended cells with Materials Studio software were used on a methane-saturated model that had been adsorbed. By deleting the methane molecule on one side, the blank layer is formed again and separated from the saturated adsorbed methane layer. SWNTs were used to drill cylindrical micropores and mesoporous pores 1 nm, 2 nm, 3 nm and 4 nm in size in the model. Atoms in the pores were deleted, and then other atoms were hydrogenated and saturated to simulate the real cylindrical pores in coal and study the diffusion behavior of methane in micropores and mesoporous pores.

We simulated the diffusion of methane with pore sizes of 1 nm, 2 nm, 3 nm and 4 nm, temperature of 303.15 K and pressures from 0.5 to 15.0 MPa to verify the effect of pressure on diffusion. Furthermore, we simulated the diffusion of methane with pore sizes of 1 nm, 2 nm, 3 nm and 4 nm, pressure of 5.0 MPa and temperatures of 283.15 K, 303.15 K, 323.15 K, 343.15 K and 363.15 K to illustrate the effect of temperature on the diffusion of methane.

In this paper, the dynamics of the system are carried out using the Forcite module of Material Studio to ensure sufficient time to form a stable linear relationship between MSD and time. Firstly, a 500 ps NVE ensemble was used for crystal relaxation to ensure the optimal structure. Then, the 500 ps NVT ensemble was used to balance the system, and finally, the 500 ps NPT ensemble was used for molecular dynamics simulation. MSD stands for mean square displacement and refers to the fact that liquid and gas molecules do not stay in a fixed position but are constantly moving. The MSD represents the degree of deviation between the position of the molecules in the system after their movement and their starting position in the simulation time. There is a correspondence between the magnitude of the value and the diffusion coefficient of the atoms. The MSD curves for different systems can be obtained through analysis of the Forcite module after optimization. The diffusion coefficients are calculated using the mean square displacement curve and the Einstein method, where the Einstein equation is given by [38,39,52].

$$D = \frac{1}{6N} \lim_{t\to\infty} \frac{d}{dt} \left\langle \sum_{i=1}^{N} [r_i(t) - r_i(0)]^2 \right\rangle \tag{3}$$

where D is the diffusion coefficient, m^2/s; N is the number of molecules of the adsorbent; t is the simulation time, ps; and r_i (t) and r_i (0) are the position vectors of adsorbent i at moment t and the initial moment, respectively. The MSD curve is fitted linearly, and the slope k obtained is the diffusion coefficient D; Equation (3) is simplified to

$$D = \frac{k}{6} \tag{4}$$

3. Results and Discussion

3.1. Ultimate Analysis and Proximate Analysis Results

The results of ultimate analysis and proximate analysis are shown in Table 1. As can be seen from Table 1, the ultimate and approximate analyses of the FK–3 sample were close to the average, so we chose the FK–3 sample for FTIR, XPS and ^{13}C NMR analyses in this study.

Table 1. Property analyses of the coals.

Sample	Proximate Analysis (wt%)				Ultimate Analysis (daf, wt%)					Atomic Ratio		Ro (%)
	M_{ad}	A_{ad}	V_{ad}	FC_{ad}	C	H	O	N	S	H/C	O/C	
FK–1	3.06	15.24	29.72	51.98	78.89	4.71	15.38	0.82	0.20	0.72	0.15	0.79
FK–2	1.12	15.25	34.15	49.48	83.72	5.32	8.83	1.86	0.27	0.76	0.08	0.83
FK–3	1.82	18.63	32.55	47.00	80.46	5.51	12.32	1.71	0	0.82	0.11	0.81
FK–4	1.15	10.11	35.64	53.10	76.14	4.59	17.95	1.32	0	0.72	0.18	0.76
FK–5	0.99	19.59	36.09	43.33	84.11	5.19	8.82	1.53	0.35	0.74	0.08	0.90
Average	1.63	15.76	33.63	48.98	80.66	5.06	12.66	1.45	0.16	0.75	0.12	0.82

3.2. Molecular Structure Construction

3.2.1. ^{13}C NMR Spectra Analysis

The ^{13}C NMR profiles and chemical shift assignments of the FK−3 coal are shown in Figure 2. Based on the observation that there are four peaks in the NMR spectrum, 18–27 ppm corresponds to aliphatic $-CH_3$, $-RCH_3$ and $-CH_2$, which indicates the presence of some number of aliphatic chains in the coal structure. The prominent peak at 110–150 ppm corresponds to the chemical shift of aromatic carbon, indicating that aromatic carbon accounts for the most significant proportion of organic carbon in the coal in total. The peak at 150–190 ppm corresponds to carboxyl carbon and that at 210–220 ppm corresponds to carbonyl carbon, indicating the presence of a large number of oxygen atoms in the coal molecule [55,61–67], which is consistent with the results of the elemental analysis (15.38% oxygen).

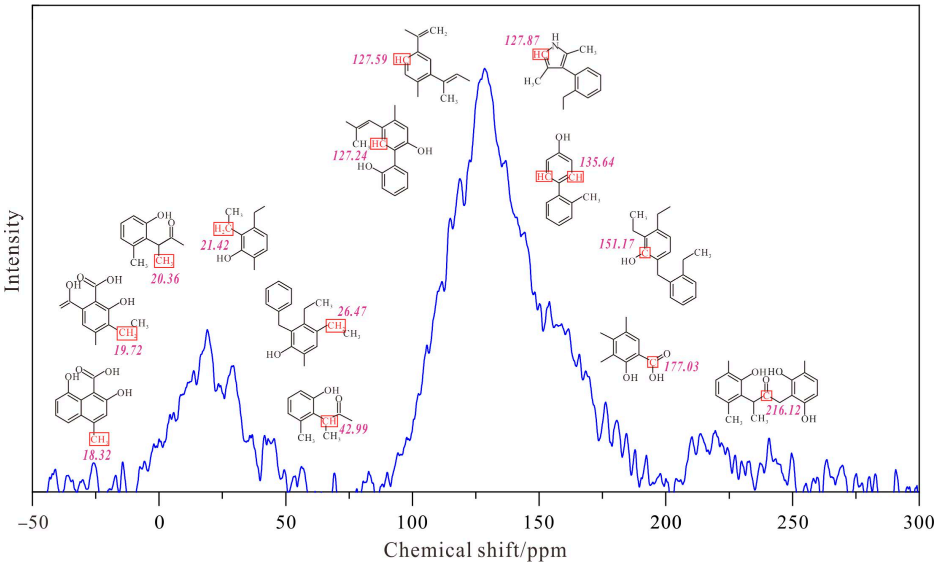

Figure 2. The ^{13}C nuclear magnetic resonance profile of the FK–3 coal with chemical shift assignments.

3.2.2. FTIR Spectra Analysis

The FTIR profiles of the Fukang coal are shown in Figure 3. The peaks located at 700–900 cm^{-1}, 1171 cm^{-1}, 1373 cm^{-1}, 1430 cm^{-1}, 1591 cm^{-1}, 1678 cm^{-1}, 2865 cm^{-1}, 2920 cm^{-1} and 3211 cm^{-1} correspond to $(C–H)_{ar}$, C–O, $–CH_3$, $–CH_2$, C=C, C=O, $–CH_2$, $–CH_3$ and –OH, respectively, evidence of the presence of moisture in the coal samples can be found from the peaks present in the 3000–3300 cm^{-1} wave number range, and the relatively consistent information on coal structure obtained in Figures 2 and 3 are a good indication that both experiments have an essential role in reconstructing the molecular structure of coal [18,56,66,67].

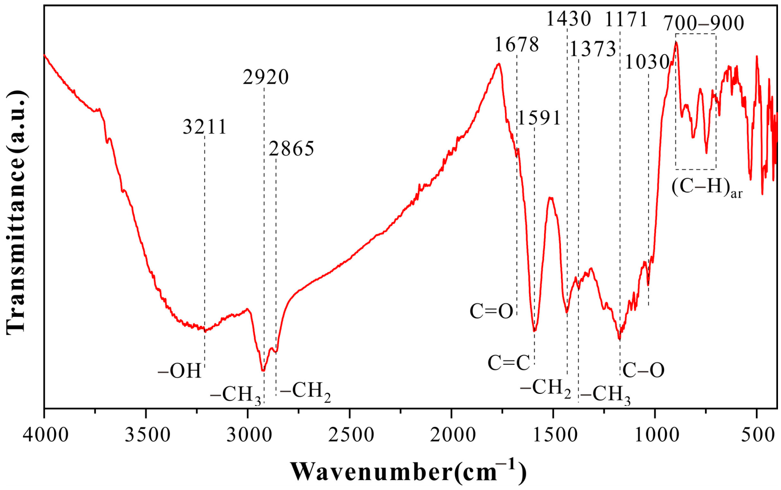

Figure 3. The Fouriertransform interferometric radiometer profile of the FK–3 coal with wavenumber assignments.

3.2.3. XPS Spectra Analysis

Figure 4 shows the XPS scans of C, N and O. To identify and quantify statistical information on the different types of chemical functional groups, these XPS narrow scan spectra were fitted using Avantage software (version v5.948).

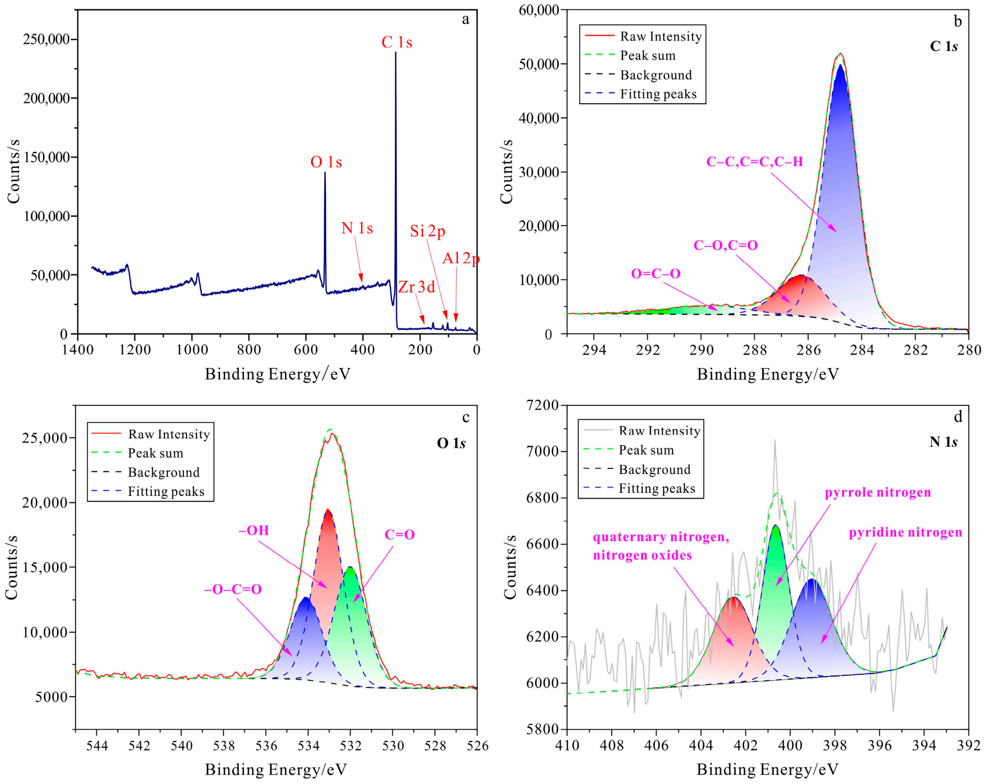

Figure 4. (**a**) X–ray photoelectron spectroscopy wide scan; (**b**) C 1s scan; (**c**) O 1s scan; (**d**) N 1s scan of the FK–3 coal.

The XPS wide scan spectrum in Figure 4a shows the presence of C, O, N, Zr, Si and Al atoms in the Fukang coal. The higher content of C, O and N atoms are the main constituent atoms on the surface of the coal particles, but the lower content of Si, Al and

Zr are negligible. The relative content of C atoms is the highest at 79.40%, followed by O atoms at 15.25% and N atoms at only 1.67%. (Table 2).

Table 2. Relative contents of different atoms based on XPS wide scan spectrum.

Name	Peak BE	FWHM eV	Area (P) CPS. eV	Atomic Fraction %
C 1s	285.06	2.75	623,376.77	79.40
O 1s	532.99	3.28	347,508.17	15.25
N 1s	400.14	5.54	24,505.92	1.67
Zr 3d	179.18	1.62	1213.02	0.01
Si 2p	103.25	3.16	21,673.02	2.29
Al 2p	75.28	3.11	8251.23	1.38

From Table 3 and Figure 4b, the carbon atoms in the form of three bonds C–C, C=C and C–H account for 79.90% of the total carbon, and such carbon atoms mainly exist in the chemical groups of aromatic rings and aliphatic chains. The carbon atoms in –C–O– and C=O account for 13.40%, mainly in the functional groups of alcoholic hydroxyl, phenolic hydroxyl, ether or carbonyl. There are also some carbon atoms in the form of O=C–O, accounting for 6.70% of the total carbon, indicating that there are trace carboxyl groups in the coal structure.

Table 3. Peak-fitting results of C 1s scan spectrum.

Position (eV)	Area	FWHM (eV)	Percentage	Assignment [18]
284.80	79,131.47	1.53	79.90%	C–C, C=C, C–H
286.36	13,268.87	1.78	13.40%	C–O, C=O
289.62	6633.19	3.50	6.70%	O=C–O

According to the results in Figure 4c and Table 4, the oxygen atoms can be classified into three types: C=O, –OH and –O–C=O, and the oxygen in the hydroxyl group atoms accounted for the highest proportion at 44.57%, followed by oxygen atoms in carbonyl groups and oxygen atoms in carboxyl groups, accounting for 32.97% and 22.46%, respectively.

Table 4. Peakfitting results of O 1s spectrum.

Position (eV)	Area	FWHM (eV)	Percentage	Assignment [18]
532	17,927.60	1.87	32.97%	C=O
533.03	24,232.86	1.84	44.57%	–OH
534.08	12,212.12	1.74	22.46%	–O–C=O

From the results in Figure 4d and Table 5, the nitrogen atoms mainly exist in the form of pyrrolic nitrogen and pyridine nitrogen, accounting for 70.37% of the total nitrogen atoms. In addition, some other forms of nitrogen atoms, such as quaternary nitrogen atoms or nitrogen atoms in nitrogen oxide compounds, account for 29.63% of the total nitrogen atoms.

Table 5. Peak-fitting results of N 1s spectrum.

Position (eV)	Area	FWHM (eV)	Percentage	Assignment [18]
399.05	974.51	2.20	34.41%	pyridine nitrogen
400.65	1018.45	1.46	35.96%	pyrrole nitrogen
402.57	839.14	2.16	29.63%	quaternary nitrogen, nitrogen oxides

3.2.4. Construction and Validation of 2D Coal Molecular Structure

The 2D chemical molecular structure of Fukang coal was determined according to XPS, FTIR and ^{13}C NMR data, as shown in Figure 5a. Figure 5b compares the ^{13}C NMR data estimated based on the 2D structure and the experimental NMR data. The data obtained from the calculation results agree with the experimental NMR data. The molecular formula of the constructed coal structure is $C_{179}H_{155}NO_{44}$, and the total molecular weight is 3021.

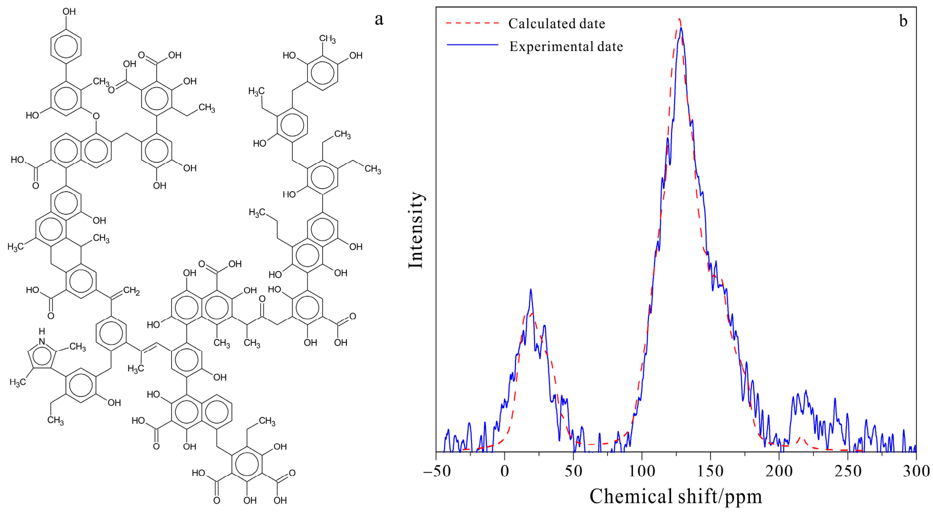

Figure 5. (**a**) Two-dimensional molecular structure of the FK–3 coal; (**b**) comparison of experimental data and calculated data.

3.2.5. Construction of 3D Coal Molecular Structure

In Figure 6a, the 3D coal structure consists of 14 coal macromolecules with a unit cell size of 3.73 × 3.73 × 3.73 nm and contains 5306 atoms ($C_{2506}H_{2170}N_{14}O_{616}$). In this study, a 1 nm blank slit layer was constructed (Figure 6b) to simulate the adsorption of methane at different temperatures (303.15 K, 323.15 K, 343.15 K and 363.15 K) and pressures (increased from 0.5 to 1.0 to 2.0 to 15.0 MPa). Supercell module was used to construct supercells on the basis of models of methane adsorption at different saturation levels. The supercell was composed of 112 coal molecules, with a cell size of 7.47 × 7.47 ×13.21 nm and 42448 atoms ($C_{20048}H_{17360}N_{112}O_{4928}$) (Figure 7a).

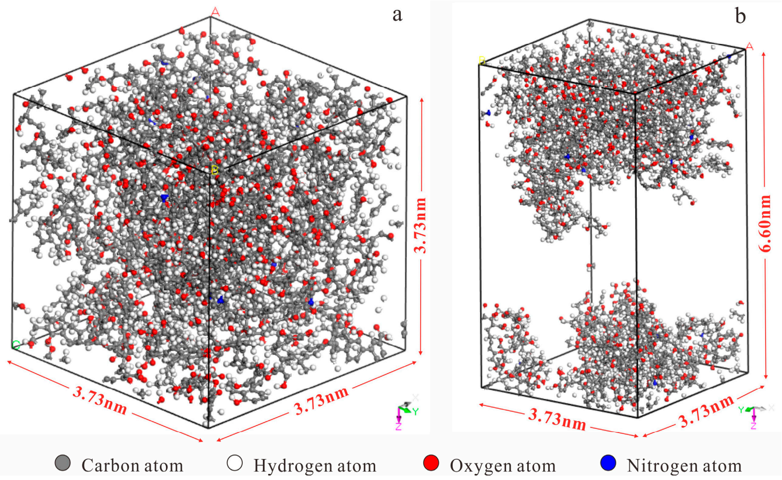

Figure 6. (**a**) Three-dimensional molecular structure model of the FK–3 coal.; (**b**) The 3D molecular structure model added with 1 nm blank slit blank layer.

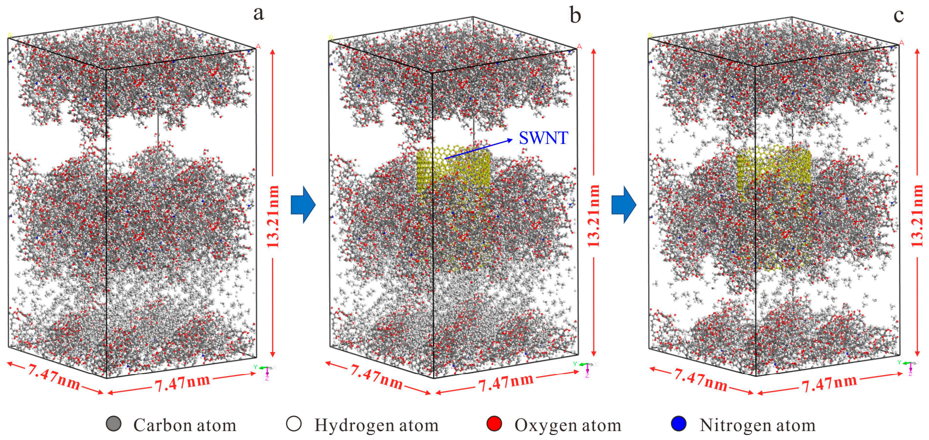

Figure 7. (**a**) Methane diffusion process at different temperatures, pressures and pore sizes in the molecular structure model of FK–3 coal. Molecular structural model; (**b**) snapshot of methane before diffusion in the molecular structural model; (**c**) and snapshot of methane after diffusion through a single-walled carbon nanotube (SWNT) in the molecular structure model.

Figure 7 shows the constructed diffusion model (Figure 7a) and snapshots before (Figure 7b) and after diffusion (Figure 7c). In Figure 7a, there were two slits in the supercell; the lower slits layer contained saturated adsorbed methane molecules, while the upper slits layer was blank. In this study, SWNTs were used to drill holes in the coal molecular layer in the middle of Figure 7a, and cylindrical holes 1 nm, 2 nm, 3 nm and 4 nm in size were drilled. Figure 7b shows the diffusion model after drilling cylindrical holes, and Figure 7c shows the simulation through molecular dynamics. methane molecules in the slit layer at the bottom of the model migrated to the slit layer at the top of the model through the cylindrical hole in the middle. Finally, methane in the slit layer reached a dynamic equilibrium.

3.3. Methane Adsorption Results

Figure 8 shows the curves of absolute adsorption capacity and excess adsorption capacity of methane under different temperature and pressure conditions. It can be seen from Figure 8a that at the same temperature, the absolute adsorption capacity of methane increases rapidly with the increase in fugacity and then tends to decrease. The absolute adsorption capacity decreases with the increase in temperature. This is because adsorption is an exothermic process. The kinetic energy of the methane molecule increases with the increase in temperature, which makes it easier for the methane molecule to decrease adsorption on the pore wall.

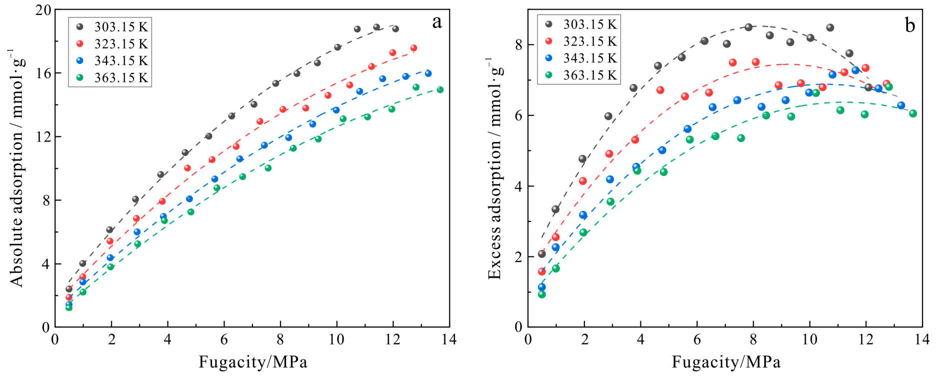

Figure 8. (**a**) The relationship between fugacity and absolute adsorption capacity at different temperatures.; (**b**) The relationship between fugacity and excess adsorption capacity at different temperatures.

As can be seen from Figure 8b, when the temperature was 303.15 K, the adsorption capacity of methane increased rapidly when the fugacity was less than 5 MPa and slowly increased when the fugacity was 5–7.83 MPa. When the fugacity was 7.83 MPa, the excess adsorption capacity reached the maximum value of 8.49 mmol/g and reached the saturated adsorption state. When the fugacity was greater than 7.83 MPa, the excess adsorption capacity of methane gradually decreased because, with the increase in fugacity, the kinetic energy of methane molecules also increases, thus decreasing the adsorption on the pore wall and transforming the adsorbed gas into free gas. Under the same fugacity, the excess adsorption capacity decreases with the increase in temperature, and with the increase in temperature, the fugacity required to reach the maximum excess adsorption capacity gradually increases. When the temperature was 323.15 K and the fugacity was 8.09 MPa, the maximum excess adsorption capacity was 7.51 mmol/g. When the temperature was 343.15 K and the fugacity was 11.63 MPa, the maximum excess adsorption capacity was 7.28 mmol/g. However, when the temperature was 363.15 K, the fugacity needed to reach 12.81 MPa to achieve the maximum excess adsorption capacity of 6.81 mmol/g.

To further investigate the methane adsorption characteristics in coal, it is necessary to explore the spatial distribution of methane molecules in the slit pore model. Figure 9 shows the relative concentration distribution of methane under different pressure conditions in the (0 0 1) face of the model. The purple, red, blue and green lines in Figure 9a represent relative concentration distribution curves at pressures of 1.0 MPa, 5.0 MPa, 9.0 MPa and 15.0 MPa, respectively. Figure 9b shows snapshots of methane spatial distribution at pressures of 1.0 MPa, 5.0 MPa, 9.0 MPa and 15.0 MPa. It is clear from Figure 9a that the relative concentration of methane in the coal molecular space gradually increases as the pressure increases from 1.0 MPa to 15.0 MPa. However, the concentration of methane in the slit layer increases while the concentration of methane adsorbed on the surface of coal molecules on both sides tends to decrease. When the pressure is low, methane molecules are preferentially adsorbed in the surface pores of the coal molecules rather than in the slit layer, and this phenomenon can also be seen well in Figure 9b. This is because as the pressure increases, the kinetic energy of the methane molecules increases and the methane molecules diffuse out of the gravitational pull of the coal molecules into the slit layer. This once again confirms the existence of regional differences in the adsorption of methane in the slit pores of coal [42].

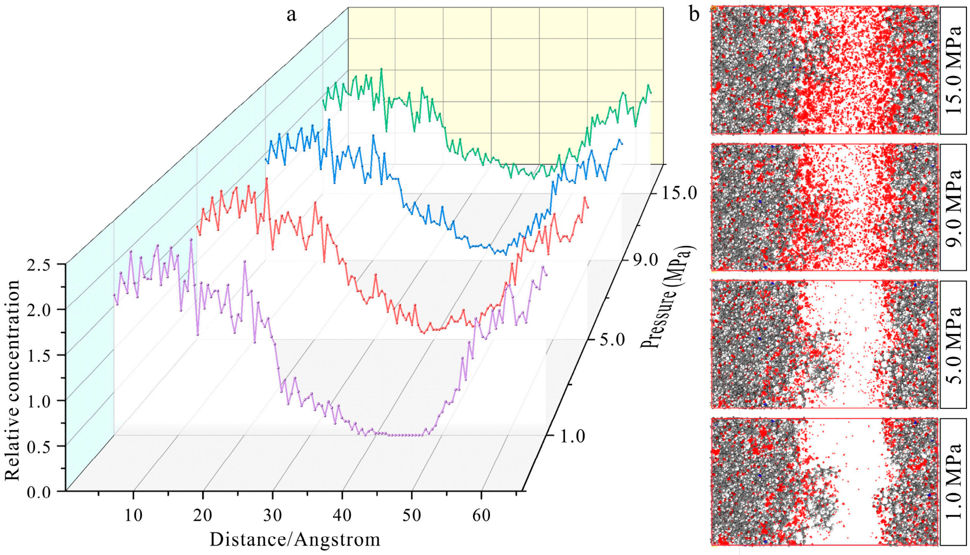

Figure 9. (**a**) The relative concentration distribution of CH_4 in the coal model along the z-axis at different pressures.; (**b**) Snapshot of CH_4 molecules (red dots) concentration distribution in coal model at different pressures.

Figure 10 shows the relative concentration and spatial distribution of methane at different temperatures. Figure 10a shows the relative concentration distribution curves of methane molecules in the (0 0 1) face of the slit pore model at different temperatures. The purple, red, blue and green lines in Figure 10a represent the relative distribution curve of methane in the coal model at temperatures of 303.15 K, 323.15 K, 343.15 K and 363.15 K, respectively, while the snapshot of methane spatial distribution in the coal model at the corresponding temperature is shown in Figure 10b. It can be seen from Figure 10a that as the temperature increases from 303.15 K to 363.15 K, the molecular concentration of methane in the slit layer shows a downward trend, while the concentration of methane adsorbed by coal molecules on both sides of the slit layer shows an upward trend, which is consistent with the phenomenon seen in Figure 10b. This is because the adsorption of gases is an exothermic process and the increase in temperature is not conducive to the adsorption of methane on the coal surface.

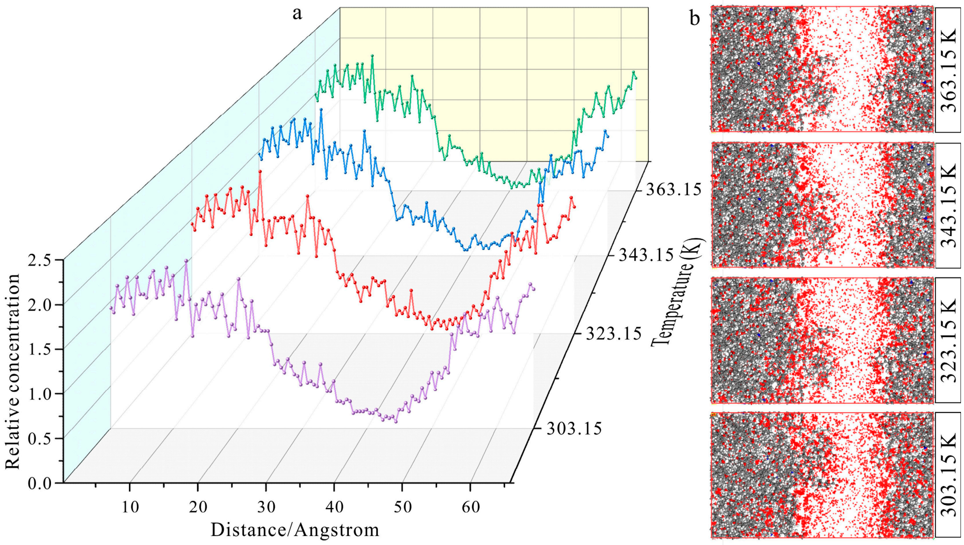

Figure 10. (**a**) The relative concentration distribution of CH_4 in the coal model along the z-axis at different temperatures.; (**b**) Snapshot of CH_4 molecules (red dots) concentration distribution in coal model at different temperatures.

3.4. Methane Diffusion Results

3.4.1. Mean Square Displacement (MSD)

The effect of different pore sizes, pressures and temperatures on the diffusion characteristics of methane was investigated by molecular dynamics simulations, and the relationship between the MSD of the gas and the simulation time was obtained, as shown in Figure 11.

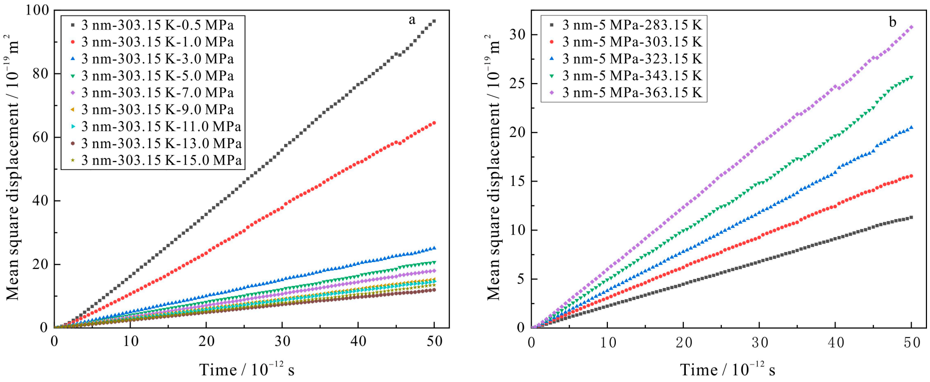

Figure 11. (**a**) Mean square displacement for FK–3 coal, calculated from molecular dynamics simulations, as function of time for different pressures; (**b**) and temperatures.

Figure 11a shows the MSD curves of methane under different pressures when the diffusion aperture is 3 nm and the temperature is 303.15 K. The results show that the slope of the MSD curve is the highest when the pressure is 0.5 MPa, the slope of the MSD curve is the minimum when the pressure is 15.0 MPa and the slope of the MSD curve decreases with increasing pressure. Figure 11b shows the MSD curves of methane at different temperatures when the diffusion aperture is 3 nm and the pressure is 5.0 MPa. The results show that the slope of the MSD curve is the highest when the pressure is 363.15 K, the slope of the MSD curve is the minimum when the pressure is 283.15 K and the slope of the MSD curve increases with the increase in temperature.

Figure 12a shows the methane MSD curve under different pressures with a diffusion pore size of 1nm and temperature of 303.15 K, indicating that the slope of the MSD curve decreases rapidly first and then tends to decrease slowly with the increase in pressure. Figure 12b shows the MSD curve with different pore sizes under the same temperature and pressure conditions. The slope of the MSD curve increases with the increase in pore size, but the change is not significant, indicating that methane diffusion mainly occurs in micropores and the effect of pore size on methane diffusion is not significant.

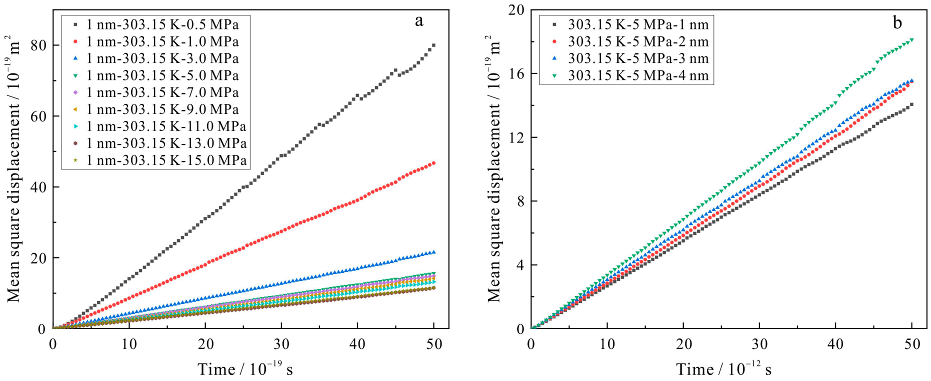

Figure 12. Mean square displacement for FK–3 coal, calculated from molecular dynamics simulations, as function of time for different pressures (**a**) and pore sizes (**b**).

3.4.2. Diffusion Coefficient

According to Equations (3) and (4), the gas diffusion coefficient in different pores can be obtained. The diffusion coefficient is a commonly used physical quantity to characterize the law of gas migration in a medium [38]. This article quantitatively characterized the diffusion law of methane. From Figure 13a, the diffusion coefficient of methane tends to decrease with increasing pressure. However, as can be seen in Figure 13b, as the temperature increased, the diffusion coefficients of methane showed an increasing trend.

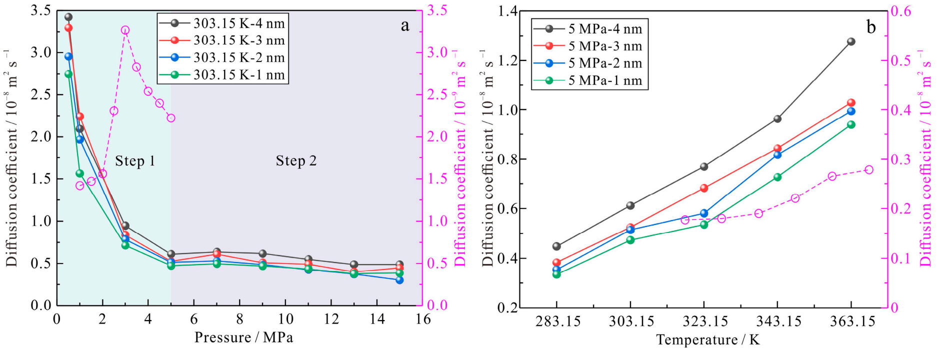

Figure 13. Diffusion coefficients for FK–3 coal, calculated from molecular dynamics simulations, as function of methane pressure (**a**) and temperature (**b**). Data from Liu et al. [37] are plotted as dashed lines for comparison.

As shown in Figure 13a, the diffusion coefficient of methane increased from 2.75×10^{-8} m^2/s to 3.42×10^{-8} m^2/s at a temperature of 303.15 K, an increase in pore size from 1 nm to 4 nm and a pressure of 0.5 MPa, but at a pressure of 15.0 MPa, the diffusion coefficient of methane only increased from 0.38×10^{-8} m^2/s to 0.49×10^{-8} m^2/s, showing that the diffusion coefficient tends to decrease with increasing pressure. The variation in the diffusion coefficient of methane in coal can be divided into two stages. The first stage is a rapid decrease stage, from 0.5 MPa to 5.0 MPa, where the diffusion coefficient of methane dropped sharply and the diffusion coefficient decreased by 82.89% on average; the second stage is a declining stage, from 5.0 MPa to 15 MPa, where the diffusion coefficient tended to be less but the diffusion coefficient decreased only by 23.74% on average. In the range of 1 nm ~ 4 nm pore size, the diffusion coefficient is consistent. Under the same pressure, the diffusion coefficient increases with the increase in pore diameter. The diffusion coefficient calculated in Figure 13a is compared with that of Liu et al. [37]. The diffusion coefficient calculated by Liu et al. is also divided into two stages: 1.0MPa–3.0 MPa is the rapid rise stage, and 3.0 MPa–5.0 MPa is the rapid decline stage. From Figure 13b, the pore size was increased from 1 nm to 4 nm, the pressure was 5.0 MPa and the diffusion coefficient of methane increased from 0.33×10^{-8} m^2/s to 0.45×10^{-8} m^2/s at a temperature of 283.15 K. As at a temperature of 363.15 K, the diffusion coefficient of methane increased from 0.94×10^{-8} m^2/s to 1.28×10^{-8} m^2/s. This demonstrates that as the temperature increases, the diffusion of methane tends to increase, and the larger the pore size, the stronger the diffusion of methane at the same temperature. The diffusion coefficient calculated in Figure 13b is compared with that of Liu et al. [37]. The diffusion coefficient calculated by Liu et al. increases gradually with the increase in temperature, which is consistent with the research results in this paper.

As the pressure increases, the amount and concentration of methane adsorbed by the coal increase, the increase in concentration increases the concentration difference with the external gas and the methane diffusion effect is enhanced. The adsorption of methane increases and expands the coal matrix, the original diffusion channel expands and narrows due to methane adsorption and methane diffusion is blocked, so the diffusion coefficient decreases with the increase in pressure.

3.4.3. Total Energy

As can be seen from Figure 14a, the total energy tends to increase as the pressure increases, and the larger the pore size, the smaller the total energy at the same pressure; in Figure 14b, the total energy tends to decrease as the temperature increases, and the larger the pore size, the smaller the total energy at the same temperature.

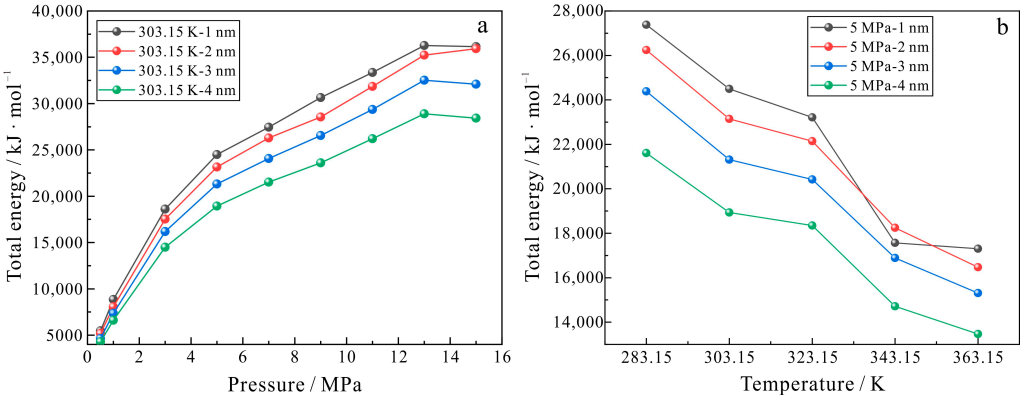

Figure 14. Total energy for FK–3 coal, calculated from molecular dynamics simulations, as function of methane pressure (**a**) and temperature (**b**).

Molecular diffusion is the process by which molecules break free from adjacent molecules' gravitational forces. In this process, molecules need to absorb heat from the outside world for conversion into kinetic energy. The greater the diffusion coefficient, the faster the molecules diffuse, the more molecules absorb heat from the external environment for conversion into kinetic energy and the smaller the total energy; conversely, the slower the diffusion, the greater the total energy, so the total energy increases with the increase in pressure, the total energy decreases with the increase in temperature and, at the same temperature and pressure, the larger the pore size, the smaller the total energy.

3.4.4. Activation Energy

The diffusion of methane in the coal structure is in fact an activation process, and the diffusion activation energy can be calculated analytically using the Arrhenius equation, which reads:

$$D = D_0 e^{-\frac{E_a}{RT}} \tag{5}$$

where D_0 represents the diffusion rate constant, m^2/s; T represents the temperature, K; E_a represents the activation energy of diffusion, J/mol; and R represents the ideal gas constant, J/(mol·K). Integrate Equation (5) to obtain Equation (6).

$$lnD = -\frac{E_a}{RT} + lnD_0 \tag{6}$$

From Figure 15, it can be seen that at 5.0 MPa, the pore sizes are 4 nm, 3 nm, 2 nm and 1 nm, the slopes of the fitted lines are −1309.55, −1269.82, −1295.71 and −1276.96, respectively and the activation energies calculated from Equation (4) are 10.89 kJ/mol, 10.56 kJ/mol, 10.77 kJ/mol and 10.62 kJ/mol, respectively.

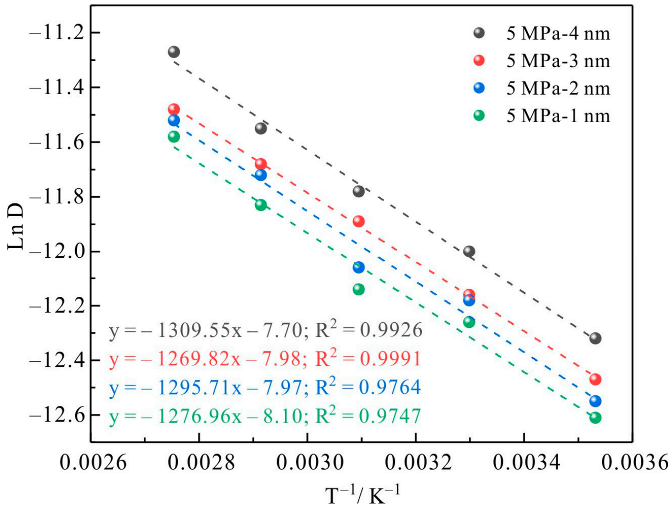

Figure 15. Activation energy with same pressure and different pores.

3.4.5. Radial Distribution Function

The radial distribution function is the spatial distribution distance for a given determinate particle from other particles, so the radial distribution function can be used both to study the ordering of matter and to describe the correlation of electrons. There are three common types of RDFs, radial distribution functions (RDFs), the approximate radial distribution function and the two-body distribution function, i.e.,

$$RDF(r) = 4\pi r^2 \rho(r) \tag{7}$$

$$G(r) = 4\pi r[\rho(r) - \rho_a] \tag{8}$$

$$g(r) = \frac{\rho(r)}{\rho_a} \tag{9}$$

where $\rho(r)$ is the number density of the radial distribution of atoms, r is the radius of the radial distribution of atoms and ρ_a is the average number density of atoms in the system.

The RDF expression is derived from diffraction intensity theory and its Fourier transform as:

$$RDF(r) = 4\pi r^2 \rho_a + \frac{2r}{\pi}\int_0^\infty s[I(s)-1]\sin(sr)ds \quad (10)$$

$$G(r) = \frac{2}{\pi}\int_0^\infty s[I(s)-1]\sin(sr)ds \quad (11)$$

$$g(r) = 1 + \frac{1}{2\pi^2 r\rho_a}\int_0^\infty s[I(s)-1]\sin(sr)ds \quad (12)$$

where $I(s) = \frac{I_n(s)-[\langle f^2\rangle - \langle f\rangle^2]}{\langle f\rangle^2}$, $s[I(s)-1] = \frac{s[I_n(s)-\langle f^2\rangle]}{\langle f\rangle^2}$, $\langle f^2\rangle = \sum_i c_i f_i^2$, $\langle f\rangle^2 = \left(\sum_i c_i f_i\right)^2$, c_i and f_i are the fraction of each type of atom and the atomic scattering factor. $I_n(s)$ is the coherent scattering intensity of an atom; $s = \frac{4\pi \sin\theta}{\lambda}$.

From Figure 16, it can be seen that at the stage of $g(r) = 0$, the truncation radius r of C–CH_4 is 0.10 nm (0.095 Å $\approx$ 0.10 nm) and the maximum peak occurs at $r = 0.11$ nm for both plots. Figure 16a demonstrates the radial distribution function for the interaction of C atoms with methane molecules at the same pore size, the same temperature and different pressures. It can be seen that the lower the pressure, the higher the peak of the curve. Figure 16b shows the radial distribution as a function of the interaction between the C atom and the methane molecule for the same pore size, the same pressure and different temperatures. The higher the temperature, the lower the peak of the curve.

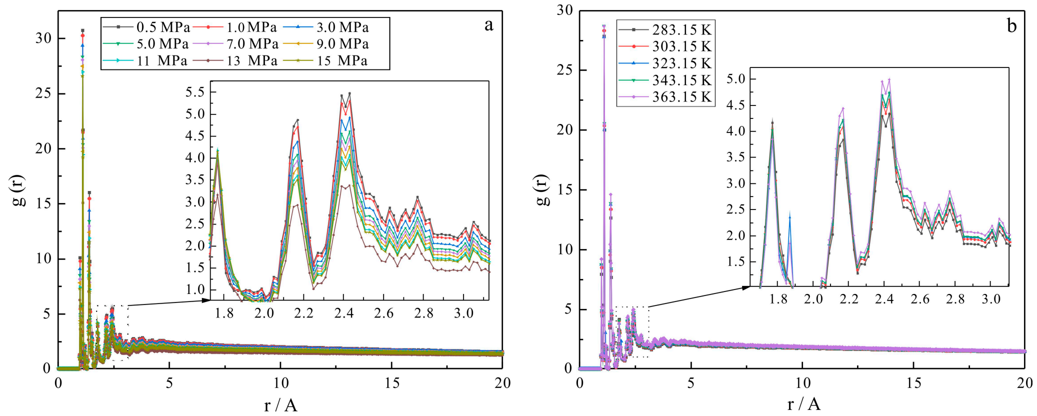

Figure 16. (**a**) Radial distribution function between methane molecules and C atoms, calculated from molecular dynamics simulations, as function of truncation radius for different pressures; (**b**) and temperatures.

At the same temperature and pore size, the lower the pressure, the faster the methane diffuses, the weaker the adsorption of methane by the coal molecules and the further the C atoms are from the methane molecules. As can be seen in Figure 16a, the peak is highest at 0.5 MPa and lowest at 15.0 MPa, further evidencing that the increase in pressure hinders the diffusion of methane. However, the temperature is the opposite of pressure, as diffusion of gas is a heat absorption process. As the temperature increases, the internal energy of the molecules is enhanced. The methane molecule breaks free from intermolecular gravitational forces and diffusion accelerates, as seen in Figure 16b, where the peak is highest at 363.15 K and lowest at 283.15 K.

In this paper, the adsorption and diffusion characteristics of methane in the low-rank coal model of the Junggar Basin are studied by using molecular simulation methods. This method is also applicable to other potential coalbed methane basins and can provide a theoretical basis for improving CBM production.

4. Conclusions

In this paper, the sorption and diffusion characteristics of methane in Fukang low-rank coal were investigated by molecular simulation. The main results are summarized as follows.

(1) The molecular structure of Fukang coal was characterized by a series of experiments including elemental analysis, FTIR, XPS and ^{13}CNMR. The molecular formula of the constructed 2D coal is $C_{179}H_{155}NO_{44}$. The 3D coal macromolecule structure model consists of 14 coal molecules and its molecular weight is 42294 ($C_{2506}H_{2170}N_{14}O_{616}$).

(2) The excess adsorption of methane shows an increase followed by a decrease with increasing pressure. However, the diffusion of methane shows two phases with increasing pressure: 0.5–5.0 MPa for a sharp decrease in the diffusion coefficient and 5.0–15.0 MPa for a slow decrease in the diffusion coefficient.

(3) The total diffusion energy increases with increasing pressure; however, the total diffusion energy tends to decrease with increasing temperature and pore size. The diffusion activation energy decreases with decreasing pore size.

(4) The radial distribution function has been used to study the radius of action of the methane and C atoms in the coal molecule. The lower the pressure, the larger the effective radius; the higher the temperature, the more significant the diffusion and the larger the effective radius.

(5) As the depth of CBM mining increases, water, carbon dioxide and nitrogen displacement methane will be further studied by molecular simulation technology, and the yield of CBM will increase dramatically.

Author Contributions: Conceptualization, J.X. and Y.L.; methodology, J.X. and J.L.; validation, J.X., and X.L.; investigation, J.X. and W.G.; resources, X.L.; data curation, J.X. and W.G.; writing—original draft preparation, J.X.; writing—review and editing, J.X. and J.L.; visualization, J.X., Y.G. and J.Y.; supervision, J.X. and X.L.; funding acquisition, J.X. and X.L. All authors have read and agreed to the published version of the manuscript.

Funding: This study was jointly supported by the National Natural Science Foundation of China (No. 41572125 and U1810201) and the Fundamental Research Funds for the Central Universities (No. 2020YJSMT02, 2021YJSMT09 and 2022YJSMT03).

Data Availability Statement: Not applicable.

Acknowledgments: We thank Jizhen Zhang (Yangtze University), Qiang Wei (Suzhou University), Jie Sun (General Prospecting Institute of China National Administration of Coal Geology), Xiaoling Wang (China University of Mining and Technology (Beijing)) and Yungang Zhao (China University of Mining and Technology (Beijing)) for their assistance in geological survey, CBM adsorption, CBM diffusion and molecular modeling. We also thank the editor and the reviewers for their helpful recommendations and constructive suggestions.

Conflicts of Interest: The authors declare no conflict of interest.

References

1. Fu, H.J.; Tang, D.Z.; Xu, T.; Xu, H.; Tao, S.; Zhao, J.L.; Chen, B.L.; Yin, Z.Y. Preliminary research on CBM enrichment models of low-rank coal and its geological controls: A case study in the middle of the southern Junggar Basin, NW China. *Mar. Petrol. Geol.* **2017**, *83*, 97–110. [CrossRef]
2. Hou, H.H.; Shao, L.Y.; Tang, Y.; Zhao, S.; Yuan, Y.; Li, Y.N.; Mu, G.Y.; Zhou, Y.; Liang, G.D.; Zhang, J.L. Quantitative characterization of low-rank coal reservoirs in the southern Junggar Basin, NW China: Implications for pore structure evolution around the first coalification jump. *Mar. Petrol. Geol.* **2020**, *113*, 104165. [CrossRef]
3. Ge, X.; Liu, D.M.; Cai, Y.D.; Wang, Y.J. Gas Content Evaluation of Coalbed Methane Reservoir in the Fukang Area of Southern Junggar Basin, Northwest China by Multiple Geophysical Logging Methods. *Energies* **2018**, *11*, 1867. [CrossRef]
4. Li, X.; Fu, X.H.; Yang, X.S.; Ge, Y.Y.; Quan, F.K. Coalbed methane accumulation and dissipation patterns: A Case study of the Junggar Basin, NW China. *J. Asian Earth Sci.* **2018**, *160*, 13–26. [CrossRef]
5. Fu, H.J.; Tang, D.Z.; Xu, H.; Xu, T.; Chen, B.L.; Hu, P.; Yin, Z.Y.; Wu, P.; He, G.J. Geological characteristics and CBM exploration potential evaluation: A case study in the middle of the southern Junggar Basin, NW China. *J. Nat. Gas Sci. Eng.* **2016**, *30*, 557–570. [CrossRef]

6. Kang, J.Q.; Fu, X.H.; Elsworth, D.; Liang, S. Vertical heterogeneity of permeability and gas content of ultra-high-thickness coalbed methane reservoirs in the southern margin of the Junggar Basin and its influence on gas production. *J. Nat. Gas Sci. Eng.* **2020**, *81*, 103455. [CrossRef]
7. Kang, J.Q.; Fu, X.H.; Gao, L.; Liang, S. Production profile characteristics of large dip angle coal reservoir and its impact on coalbed methane production: A case study on the Fukang west block, southern Junggar Basin, China. *J. Petrol. Sci. Eng.* **2018**, *171*, 99–114. [CrossRef]
8. Kang, J.Q.; Fu, X.H.; Shen, J.; Liang, S.; Chen, H.; Shang, F.H. Characterization of Coal Structure of High-Thickness Coal Reservoir Using Geophysical Logging: A Case Study in Southern Junggar Basin, Xinjiang, Northwest China. *Nat. Resour. Res.* **2022**, *31*, 929–951. [CrossRef]
9. Fu, H.J.; Tang, D.Z.; Xu, T.; Xu, H.; Tao, S.; Yin, Z.Y.; Chen, B.L.; Zhang, C.; Wang, L.L. Characteristics of pore structure and fractal dimension of low-rank coal: A case study of Lower Jurassic Xishanyao coal in the southern Junggar Basin, NW China. *Fuel* **2017**, *193*, 254–264. [CrossRef]
10. Fu, H.J.; Yan, D.T.; Yang, S.G.; Wang, X.M.; Zhang, Z.; Sun, M.D. Characteristics of in situ stress and its influence on coalbed methane development: A case study in the eastern part of the southern Junggar Basin, NW China. *Energy Sci. Eng.* **2019**, *8*, 515–529. [CrossRef]
11. Li, Y.; Zhang, C.; Tang, D.Z.; Gan, Q.; Niu, X.L.; Wang, K.; Shen, R.Y. Coal pore size distributions controlled by the coalification process: An experimental study of coals from the Junggar, Ordos and Qinshui basins in China. *Fuel* **2017**, *206*, 352–363. [CrossRef]
12. Jia, T.F.; Zhang, S.H.; Tang, S.H.; Wang, M.; Xin, D.; Zhang, Q. Characteristics and Evolution of Low-Rank Coal Pore Structure Around the First Coalification Jump: Case Study in Southeastern Junggar Basin. *Nat. Resour. Res.* **2022**, *31*, 2769–2786. [CrossRef]
13. Li, G.Q.; Yan, D.T.; Zhuang, X.G.; Zhang, Z.; Fu, H.J. Implications of the pore pressure and in situ stress for the coalbed methane exploration in the southern Junggar Basin, China. *Eng. Geol.* **2019**, *262*, 105305. [CrossRef]
14. Hou, H.H.; Liang, G.D.; Shao, L.Y.; Tang, Y.; Mu, G.Y. Coalbed methane enrichment model of low-rank coals in multi-coals superimposed regions: A case study in the middle section of southern Junggar Basin. *Front. Earth Sci.-Prc.* **2021**, *15*, 256–271. [CrossRef]
15. Liu, C.L.; Wang, X.H.; Liu, K.; Wang, J.; Guo, H.; Sun, Z.Q. Occurrence Features of Coalbed Methane in Inclined Coal Seam of Junggar Basin, Xinjiang. *Adv. Mater. Res.* **2013**, *868*, 696–699. [CrossRef]
16. Tang, S.L.; Liu, S.M.; Tang, D.Z.; Tao, S.; Zhang, A.B.; Pu, Y.F.; Zhang, T.Y. Occurrence of fluids in high dip angled coal measures: Geological and geochemical assessments for southern Junggar Basin, China. *J. Nat. Gas Sci. Eng.* **2021**, *88*, 103827. [CrossRef]
17. Song, Y.; Jiang, B.; Li, F.L. Molecular dynamic simulations of selective self-diffusion of $CH_4/CO_2/H_2O/N_2$ in coal. *IOP Conf. Ser.: Mater. Sci. Eng.* **2017**, *213*, 12014. [CrossRef]
18. Liu, Y.; Liu, S.M.; Zhang, R.; Zhang, Y. The molecular model of Marcellus shale kerogen: Experimental characterization and structure reconstruction. *Int. J. Coal Geol.* **2021**, *246*, 103833. [CrossRef]
19. Xiang, J.H.; Zeng, F.G.; Li, B.; Zhang, L.; Li, M.F.; Liang, H.Z. Construction of macromolecular structural model of anthracite from Chengzhuang coal mine and its molecular simulation. *J. Fuel Chem. Technol.* **2013**, *41*, 391–400. [CrossRef]
20. Anderson, C.J.; Tao, W.; Jiang, J.W.; Sandler, S.I.; Stevens, G.W.; Kentish, S.E. An experimental evaluation and molecular simulation of high temperature gas adsorption on nanoporous carbon. *Carbon* **2011**, *49*, 117–125. [CrossRef]
21. Billemont, P.; Coasne, B.; De Weireld, G. An Experimental and Molecular Simulation Study of the Adsorption of Carbon Dioxide and Methane in Nanoporous Carbons in the Presence of Water. *Langmuir* **2011**, *27*, 1015–1024. [CrossRef] [PubMed]
22. Zhang, W.S.; Shao, C.J.; Yang, Z.Q.; Zhou, J. Molecular Dynamics Investigation on the Adsorption of Coalbed Methane Utilizing Carbon Nanotubes under the Condition of Liquid Water. *Adv. Mater. Res.* **2012**, *616*, 877–880. [CrossRef]
23. Nguyen, V.T.; Do, D.D.; Nicholson, D. A new molecular model for water adsorption on graphitized carbon black. *Carbon* **2014**, *66*, 629–636. [CrossRef]
24. Meng, J.Q.; Zhong, R.Q.; Li, S.C.; Yin, F.F.; Nie, B.S. Molecular Model Construction and Study of Gas Adsorption of Zhaozhuang Coal. *Energ. Fuel* **2018**, *32*, 9727–9737. [CrossRef]
25. Song, Y.; Jiang, B.; Qu, M.J. Molecular Dynamic Simulation of Self- and Transport Diffusion for $CO_2/CH_4/N_2$ in Low-Rank Coal Vitrinite. *Energ. Fuel* **2018**, *32*, 3085–3096. [CrossRef]
26. Sander, R.; Connell, L.D.; Camilleri, M.; Pan, Z.J. CH_4, CO_2, N_2 diffusion in Bowen Basin (Australia) coal: Relationship between sorption kinetics of coal core and crushed coal particles. *J. Nat. Gas Sci. Eng.* **2020**, *81*, 103468. [CrossRef]
27. Cui, X.; Yan, H.; Zhao, P.T.; Yang, Y.X.; Xie, Y.T. Modeling of molecular and properties of anthracite base on structural accuracy identification methods. *J. Mol. Struct.* **2019**, *1183*, 313–323. [CrossRef]
28. Zheng, L.W.; Dong, S.N.; Tang, S.L.; Ji, Y.D.; Luo, J.Z.; Li, H.H.; Li, X.L.; Liu, C.Y.; Zeng, M.L. Molecular structure characterization of coal under the water–rock interaction in acid mine drainage (AMD). *J. Mol. Struct.* **2022**, *1251*, 132043. [CrossRef]
29. Ping, A.; Xia, W.C.; Peng, Y.L.; Xie, G.Y. Construction of bituminous coal vitrinite and inertinite molecular assisted by ^{13}C NMR, FTIR and XPS. *J. Mol. Struct.* **2020**, *1222*, 128959. [CrossRef]
30. Qian, L.; Tao, C.; Ma, C.; Xue, J.K.; Guo, F.Q.; Jia, X.P.; Yan, W.J. Construction of a Macromolecular Structure Model for Zhundong Subbituminous Coal. *J. Mol. Struct.* **2022**, *1248*, 131496. [CrossRef]
31. Zha, W.; Lin, B.Q.; Liu, T. Construction of Pingdingshan coal molecular model based on FT-IR and ^{13}C-NMR. *J. Mol. Struct.* **2022**, *1262*, 132992. [CrossRef]

32. Yin, T.T.; Liu, D.M.; Cai, Y.D.; Liu, Z.H.; Gutierrez, M. A new constructed macromolecule-pore structure of anthracite and its related gas adsorption: A molecular simulation study. *Int. J. Coal. Geol.* **2020**, *220*, 103415. [CrossRef]
33. Zhang, Z.Q.; Kang, Q.N.; Wei, S.; Yun, T.; Yan, G.C.; Yan, K.F. Large Scale Molecular Model Construction of Xishan Bituminous Coal. *Energ. Fuel* **2017**, *31*, 1310–1317. [CrossRef]
34. Zhao, D.; Liu, X.Q. Monte Carlo and molecular dynamics simulations of CH_4 molecules adsorption behavior in bituminous coal. *Int. J. Low-Carbon Tec.* **2022**, *17*, 879–887. [CrossRef]
35. Hu, H.X.; Li, X.C.; Fang, Z.M.; Wei, N.; Li, Q.S. Small-molecule gas sorption and diffusion in coal: Molecular simulation. *Energy* **2010**, *35*, 2939–2944. [CrossRef]
36. Jian, X.; Guan, P.; Zhang, W. Carbon dioxide sorption and diffusion in coals: Experimental investigation and modeling. *Sci. China Earth Sci.* **2012**, *55*, 633–643. [CrossRef]
37. Liu, J.; Li, S.K.; Wang, Y. Molecular Dynamics Simulation of Diffusion Behavior of CH_4, CO_2, and N_2 in Mid-Rank Coal Vitrinite. *Energies* **2019**, *12*, 3744. [CrossRef]
38. Long, H.; Lin, H.F.; Yan, M.; Bai, Y.; Tong, X.; Kong, X.G.; Li, S.G. Adsorption and diffusion characteristics of CH_4, CO_2, and N_2 in micropores and mesopores of bituminous coal: Molecular dynamics. *Fuel* **2021**, *292*, 120268. [CrossRef]
39. Han, J.X.; Bogomolov, A.K.; Makarova, E.Y.; Yang, Z.Z.; Lu, Y.J.; Li, X.G. Molecular Simulations on Adsorption and Diffusion of CO_2 and CH_4 in Moisture Coals. *Energ. Fuel* **2017**, *31*, 13528–13535. [CrossRef]
40. Song, G.H.; Lee, H.S.; Shin, H. Three-Dimensional Modelling of Desorbed Gas Volume and Comparison to Gas Production Rate in the Montney Plays, Western Canadian Sedimentary Basin. *Geofluids* **2021**, *2021*, 1–15. [CrossRef]
41. Hao, M.; Wei, C.M.; Qiao, Z. Effect of internal moisture on CH_4 adsorption and diffusion of coal: A molecular simulation study. *Chem. Phys. Lett.* **2021**, *783*, 139086. [CrossRef]
42. Hao, M.; Wei, C.M.; Zhang, H. Adsorption and Diffusion of Methane in Coal Slit Pores: Insights into the Molecular Level. *Energ. Fuel* **2022**, *36*, 880–886. [CrossRef]
43. Li, X.C.; Li, Z.B.; Ren, T.; Nie, B.S.; Xie, L.; Huang, T.; Bai, S.; Jiang, Y. Effects of particle size and adsorption pressure on methane gas desorption and diffusion in coal. *Arab. J. Geosci.* **2019**, *12*, 25634–25646. [CrossRef]
44. Li, Z.T.; Liu, D.M.; Cai, Y.D.; Shi, Y.L. Investigation of methane diffusion in low-rank coals by a multiporous diffusion model. *J. Nat. Gas Sci. Eng.* **2016**, *33*, 97–107. [CrossRef]
45. Liu, X.Q.; He, X.; Qiu, N.X.; Yang, X.; Tian, Z.Y.; Li, M.J.; Xue, Y. Molecular simulation of CH_4, CO_2, H_2O and N_2 molecules adsorption on heterogeneous surface models of coal. *Appl. Surf. Sci.* **2016**, *389*, 894–905. [CrossRef]
46. Meng, J.Q.; Niu, J.X.; Meng, H.X.; Xia, J.K.; Zhong, R.Q. Insight on adsorption mechanism of coal molecules at different ranks. *Fuel* **2020**, *267*, 117234. [CrossRef]
47. Ma, Q.X.; Nie, W.; Yang, S.B.; Xu, C.W.; Peng, H.T.; Liu, Z.Q.; Guo, C.; Cai, X.J. Effect of spraying on coal dust diffusion in a coal mine based on a numerical simulation. *Environ. Pollut.* **2020**, *264*, 114717. [CrossRef]
48. Li, Y.X.; Hu, Z.M.; Duan, X.G.; Wang, X.Y.; Shi, J.L.; Zhan, H.M. The general form of transport diffusivity of shale gas in organic-rich nano-slits—A molecular simulation study using Darken approximation. *Fuel* **2019**, *249*, 457–471. [CrossRef]
49. Zhao, Y.L.; Feng, Y.L.; Zhang, X.X. Molecular simulation of CO_2 /CH_4 self- and transport diffusion coefficients in coal. *Fuel* **2016**, *165*, 19–27. [CrossRef]
50. Wang, L.; Chen, X.J.; Song, Y.; Qi, L.L. Experimental Investigation on Diffusion Coefficients of CH_4 in Coal under High-Temperature and -Pressure Conditions. *ACS Omega* **2020**, *5*, 25634–25646. [CrossRef]
51. Li, G.; Meng, Z. A preliminary investigation of CH_4 diffusion through gas shale in the Paleozoic Longmaxi Formation, Southern Sichuan Basin, China. *J. Nat. Gas Sci. Eng.* **2016**, *36*, 1220–1227. [CrossRef]
52. Zhang, J.F.; Clennell, M.B.; Dewhurst, D.N.; Liu, K.Y. Combined Monte Carlo and molecular dynamics simulation of methane adsorption on dry and moist coal. *Fuel* **2014**, *122*, 186–197. [CrossRef]
53. Jing, D.J.; Meng, X.X.; Ge, S.C.; Zhang, T.; Ma, M.X.; Wang, G. Structural Model Construction and Optimal Characterization of High-Volatile Bituminous Coal Molecules. *ACS Omega* **2022**, *7*, 18350–18360. [CrossRef] [PubMed]
54. Bian, J.J.; Li, X.; Zeng, F.G.; Wang, X.L. Construction and Evaluation of a Medium-Rank Coal Molecular Model Using a Hybrid Experimental–Simulation–Theoretical Method. *Energ. Fuel.* **2019**, *33*, 12905–12915. [CrossRef]
55. Jing, Z.H.; Rodrigues, S.; Strounina, E.; Li, M.R.; Wood, B.; Underschultz, J.R.; Esterle, J.S.; Steel, K.M. Use of FTIR, XPS, NMR to characterize oxidative effects of NaClO on coal molecular structures. *Int. J. Coal Geol.* **2019**, *201*, 1–13. [CrossRef]
56. Xia, W.; Zhang, W. Characterization of surface properties of Inner Mongolia coal using FTIR and XPS. *Energy Sources Part A: Recovery Util. Environ. Eff.* **2017**, *39*, 1190–1194. [CrossRef]
57. Kawashima, H.; Takanohashi, T. Modification of Model Structures of Upper Freeport Coal Extracts Using ^{13}C NMR Chemical Shift Calculations. *Energ. Fuel* **2001**, *15*, 591–598. [CrossRef]
58. Okolo, G.N.; Neomagus, H.W.J.P.; Everson, R.C.; Roberts, M.; Bunt, J.R.; Sakurovs, R.; Mathews, J.P. Chemical–structural properties of South African bituminous coals: Insights from wide angle XRD–carbon fraction analysis, ATR–FTIR, solid state ^{13}C NMR, and HRTEM techniques. *Fuel* **2015**, *158*, 779–792. [CrossRef]
59. Sonibare, O.O.; Haeger, T.; Foley, S.F. Structural characterization of Nigerian coals by X-ray diffraction, Raman and FTIR spectroscopy. *Energy* **2010**, *35*, 5347–5353. [CrossRef]
60. Shen, Z.; Meng, Z.P. Enhancing the Efficiency of Coal Bed Methane Recovery by Injecting Carbon Dioxide Based on an Anthracite Coal Macromolecular Model and Simulation Methods. *Energ. Fuel* **2022**, *36*, 6329–6342. [CrossRef]

61. Ju, Y.W.; Jiang, B.; Hou, Q.L.; Wang, G.L.; Ni, S.Q. ^{13}C NMR spectra of tectonic coals and the effects of stress on structural components. *Sci. China Ser. D Earth Sci.* **2005**, *48*, 1418–1437. [CrossRef]
62. Wei, Q.; Tang, Y.G. ^{13}C-NMR Study on Structure Evolution Characteristics of High-Organic-Sulfur Coals from Typical Chinese Areas. *Minerals* **2018**, *8*, 49. [CrossRef]
63. Yan, J.C.; Lei, Z.P.; Li, Z.K.; Wang, Z.C.; Ren, S.B.; Kang, S.G.; Wang, X.L.; Shui, H.F. Molecular structure characterization of low-medium rank coals via XRD, solid state ^{13}C NMR and FTIR spectroscopy. *Fuel* **2020**, *268*, 117038. [CrossRef]
64. Ding, D.S.; Liu, G.J.; Fu, B. Influence of carbon type on carbon isotopic composition of coal from the perspective of solid-state ^{13}C NMR. *Fuel* **2019**, *245*, 174–180. [CrossRef]
65. Li, S.K.; Zhu, Y.M.; Wang, Y.; Liu, J. The Chemical and Alignment Structural Properties of Coal: Insights from Raman, Solid-State (13)C NMR, XRD, and HRTEM Techniques. *ACS Omega* **2021**, *6*, 11266–11279. [CrossRef]
66. Baysal, M.; Yürüm, A.; Yıldız, B.; Yürüm, Y. Structure of some western Anatolia coals investigated by FTIR, Raman, ^{13}C solid state NMR spectroscopy and X-ray diffraction. *Int. J. Coal Geol.* **2016**, *163*, 166–176. [CrossRef]
67. Wu, D.; Zhang, H.; Hu, G.Q.; Zhang, W.Y. Fine Characterization of the Macromolecular Structure of Huainan Coal Using XRD, FTIR, ^{13}C-CP/MAS NMR, SEM, and AFM Techniques. *Molecules* **2020**, *25*, 2661. [CrossRef]